International Journal of Biological Macromolecules 331 (2025) 148370

Contents lists available at ScienceDirect

International Journal of Biological Macromolecules

journal homepage: www.elsevier.com/locate/ijbiomac

Arabidopsis thaliana nicotinate mononucleotide adenylyltransferase: unveiling the molecular determinants and evolutionary origin of nicotinic acid mononucleotide recognition

Leonardo Sorci [a,*], Michele Cianci [b,*], Carlo Fortunato [b], Massimiliano Gasparrini [b], Nadia Raffaelli [b]

[a] Division of Bioinformatics and Biochemistry, Department of Science and Engineering of Matter, Environment and Urban Planning, Polytechnic University of Marche, Ancona, Italy
[b] Department of Agricultural, Food and Environmental Sciences, Polytechnic University of Marche, Ancona, Italy

ARTICLE INFO

Keywords:
NAD biosynthesis
Arabidopsis thaliana
Nicotinate mononucleotide adenylyltransferase (NaMNAT)
Site-directed mutagenesis
X-ray crystallography
Bioinformatics
Phylogeny

ABSTRACT

The pyridine nucleotide adenylyltransferase (PNAT) enzyme family is crucial for the synthesis of NAD, a pivotal cofactor in cellular metabolism. PNATs catalyze the transfer of an AMP moiety from ATP to either nicotinate mononucleotide (NaMN), forming nicotinate adenine dinucleotide, the immediate precursor to NAD, or to nicotinamide mononucleotide (NMN), directly yielding NAD. This enzyme family exhibits modular substrate specificity, comprising strictly NaMN-selective (bacterial NadD), NMN-selective (bacterial NadR and NadM), or bifunctional (mammalian PNAT and archaeal NadM). While *Arabidopsis thaliana* PNAT has been ambiguously annotated as bifunctional, our detailed kinetic analysis definitively establishes its strict NaMN preference, analogous to bacterial NadD. By integrating bioinformatics and X-ray crystallography of the enzyme in its apo and NaMN-bound forms, we elucidate the structural basis for NaMN selectivity, which differs from bacterial NadD. In plants, a positively charged residue (Arg106 in *A. thaliana* NaMN adenylyltransferase, NaMNAT) ensures NaMN specificity by counteracting the negative charge of the nicotinate moiety. Site-directed mutagenesis confirms the essential role of Arg106 in NaMN recognition and catalysis. Our findings support the extension of this functional assignment across Archaeoplastida. Furthermore, phylogenetic analysis reveals the complex and intertwined evolution of bacterial and plant NaMNATs, shaped by ancient gene transfers from cyanobacteria.

1. Introduction

NAD(P) cofactors and their reduced counterparts, NAD(*P*)H, are ubiquitous in all living organisms, including plants, where they play a critical role in regulating the cellular redox state, energy production, biosynthetic reactions, and photosynthesis [1]. NAD is also actively hydrolyzed at its N-glycosidic bond for regulatory purposes by ADP-ribose (ADPR) cyclases, sirtuins, mono- and poly-ADPR polymerases [2,3]. Plants maintain NAD homeostasis, which is crucial for proper cellular function, through both de novo synthesis and salvage pathways that recycle nicotinamide (Nam) (Fig. 1). The current understanding of plant NAD biosynthesis primarily derives from studies on the model organism *Arabidopsis thaliana*, with limited data available from other plant species [1,4]. Unlike other eukaryotes, which primarily synthesize NAD de novo from tryptophan, plants adopt the canonical prokaryotic pathway that converts the aspartate (Asp) precursor into nicotinate mononucleotide (NaMN) in three steps [5]. NaMN represents a crucial intermediate in plant NAD synthesis, as it stands at the crossroads of de novo and nicotinate (Na) or Nam salvage/recycling pathways (Fig. 1). Nam salvage begins with its deamidation to Na through the enzyme nicotinamidase, for which three active isoforms have been identified in *A. thaliana* [6,7]. Na can also enter the plant cell from the extracellular environment via the high-affinity membrane transporter NiaP, as demonstrated by radiometric uptake assays [8]. Inside the cell, Na is converted to NAD via the classic Preiss–Handler pathway. First, Na is converted to NaMN by the enzyme nicotinate phosphoribosyltransferase (NaPRT), which is encoded by two highly similar homologs (88 % sequence identity) in *A. thaliana* and other plant genomes [9,10], suggesting a relatively recent gene duplication. NaMN is then adenylated to nicotinate adenine dinucleotide (NaAD) by NaMN adenylyltransferase

* Corresponding authors.
E-mail addresses: l.sorci@staff.univpm.it (L. Sorci), m.cianci@staff.univpm.it (M. Cianci).

https://doi.org/10.1016/j.ijbiomac.2025.148370
Received 13 July 2025; Received in revised form 11 October 2025; Accepted 16 October 2025
Available online 16 October 2025

(NaMNAT) [11,12], and finally NaAD is amidated to NAD by a glutamine-dependent NAD synthetase.

The adenylation reaction constitutes a pivotal step in NAD biosynthesis, catalyzed by a family of enzymes with diverse substrate specificity, collectively classified as pyridine nucleotide adenylyltransferases (PNATs) [13,14]. Some PNAT enzymes, such as those in humans [15] and archaea [16], and certain bacterial NadM orthologues [17] are bifunctional, efficiently adenylating both NaMN and its amidated form nicotinamide mononucleotide (NMN). In contrast, other PNAT enzymes are strictly substrate-specific, acting only, or preferentially, on either NaMN (bacterial NadD family) or NMN (NadM in the *Francisella* genus [18] and bacterial NadR family [19]).

This functional versatility enables bifunctional and NMN-specific adenylyltransferase to synthesize NAD directly from the NMN formed from Nam via the enzyme nicotinamide phosphoribosyltransferase (Nampt). Nampt orthologs, known as NadV in bacteria, have been identified in diverse bacterial species, as well as in vertebrates and humans, but are absent in plants. Instead, in plants, nicotinamide is deamidated by nicotinamidase and rerouted to the Preiss–Handler pathway, underscoring the absence of a nondeamidating salvage route [6] (Fig. 1).

All major bioinformatic protein databases assign to the *A. thaliana* PNAT enzyme, encoded by the gene *At5g55810*, a bifunctional NMN/NaMN adenylyltransferase role. In this study, to clarify the function of this central metabolic enzyme in plants, we conducted an in-depth kinetic, mutational, and structural characterization of *A. thaliana* PNAT, revealing a strict preference for NaMN, which is consistent with the genomic reconstruction of NAD metabolism in plants. Bioinformatics and phylogenetic analyses further indicated distinct yet related evolutionary paths leading to NaMN specificity in both bacterial NadD and plant NaMNAT families. Moreover, our examination of NAD-related genes in *A. thaliana* identified additional enzymes that may recycle NMN, formed through Nudix hydrolase activity, back into NAD via the Preiss–Handler pathway (Fig. 1). In essence, our findings contribute to a refined understanding of downstream NAD biosynthesis in plants.

2. Materials and methods

2.1. Protein expression and purification

The *Arabidopsis thaliana* NaMNAT open reading frame (ORF; locus *At5g55810*, UniProt ID: F4K687) was amplified from Incyte clone 701,546,631 and subcloned into the pET-28a expression vector using the *Nde*I and *Sal*I restriction sites.

For recombinant protein production, freshly transformed *E. coli* BL21 (DE3) cells were used to inoculate a 600 mL culture of LB medium and grown at 37 °C with shaking (200 rpm). When the culture reached an OD_{600} of 0.8, expression was induced with 1 mM isopropyl β-D-1-thio-galactopyranoside. Following an overnight incubation at 37 °C, the cells were harvested by centrifugation (6000 ×*g*, 10 min, 4 °C), and the resulting pellets were stored at −80 °C until use.

Protein purification was carried out at room temperature using a Bio-Rad FPLC system equipped with a 1 mL HisTrap FF column (Ni-NTA resin). Cell pellets were resuspended in lysis buffer (50 mM HEPES/NaOH (pH 7.5), 300 mM NaCl, 10 mM imidazole, 2 mM Tris(2-carboxyethyl)phosphine (TCEP), 1 mM phenylmethanesulfonyl fluoride, and protease inhibitor cocktail), and lysed by three passages through a French pressure cell (18,000 psi). Cell debris was removed by centrifugation (20,000 ×*g*, 30 min, 4 °C), and the clarified supernatant was applied to the equilibrated Ni-NTA column (equilibration buffer: 50 mM HEPES/NaOH (pH 7.5), 300 mM NaCl, 10 mM imidazole, 2 mM TCEP). Unbound proteins were removed by washing the column with 10 column volumes (CV) of equilibration buffer, followed by 15 CV of buffer containing 100 mM imidazole. Bound *At*NaMNAT was eluted with a 15 CV linear imidazole gradient (100–350 mM) in equilibration buffer. The eluted fractions containing *At*NaMNAT were desalted using a PD-10 Sephadex G-25 column equilibrated with 50 mM HEPES/NaOH (pH 7.5), 300 mM NaCl, and 2 mM TCEP, and stored at −20 °C.

*At*NaMNAT purity was assessed by SDS-PAGE [20], and its concentration was determined using the Bradford assay with bovine serum albumin (BSA) as the standard [21].

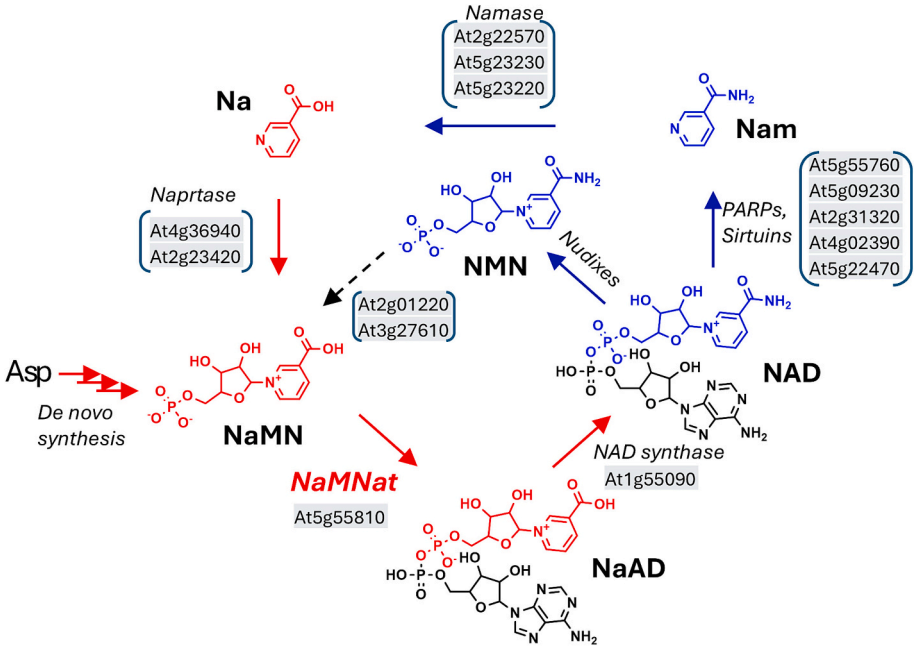

Fig. 1. NAD metabolism in *Arabidopsis thaliana*. Steps of the deamidated biosynthesis pathway (including de novo synthesis and the Preiss–Handler pathway) are shown with red arrows. For clarity, only substrates and products containing the pyridine moiety are shown for each reaction. NAD-consuming reactions and subsequent recycling of nicotinamide via nicotinamidases are shown in blue. The dotted arrow represents a hypothetical recycling route of NMN via a bacterial-like NMN deamidase activity (see text for details).

2.2. Enzyme activity assays

To monitor enzyme expression and purification, NMN adenylyltransferase activity was measured using a coupled spectrophotometric assay that links the NAD formation from NMN to NADH production. The reaction mixture contained 32 mM HEPES/NaOH (pH 7.5), 0.46 % (*v*/v) ethanol, 50 mM semicarbazide, 10 mM $MgCl_2$, 0.03 mg/mL alcohol dehydrogenase, 0.6 mg/mL BSA, 1 mM ATP, 1 mM NMN, and a proper amount of enzyme. Enzyme activity was calculated by measuring the increase in NADH absorbance at 340 nm.

For catalytic and kinetic characterization, we used an HPLC-based assay. Reaction mixtures contained 50 mM HEPES/NaOH (pH 7.5), 10 mM $MgCl_2$, appropriate amounts of the enzyme, along with ATP and either NMN or NaMN at different concentrations. Reactions were carried out at 37 °C and quenched after 5 or 10 min by adding $HClO_4$ to a final concentration of 0.6 M. The samples were then kept on ice for 10 min and centrifuged for 2 min at 20,000 ×g. The resulting supernatants were neutralized with 1 M K_2CO_3, stored at −80 °C for 20 min, centrifuged again under the same conditions, and analyzed using a Supelcosil LC-18-S column to quantify NAD or NaAD formation as described previously [22]. Product identity was confirmed by coelution with authentic standards.

One unit (U) of NMNAT or NaMNAT is defined as the amount of enzyme catalyzing the synthesis of 1 μmol of NAD or NaAD per minute at 37 °C from NMN or NaMN, respectively.

2.3. Kinetic analysis

Steady-state kinetic analyses of *At*NaMNAT and the R106A mutant were performed by varying one substrate (NaMN, NMN, or ATP) while keeping the co-substrate at a fixed, saturating concentration (5–10 mM). Initial rates were measured using the HPLC-based assay, ensuring linear reaction progress for up to 10 min with less than 5 % substrate consumption. Apparent kinetic parameters (K_m and k_{cat}) were obtained by fitting initial rate data to the Michaelis-Menten equation using Prism 7.05 (GraphPad).

2.4. Crystallization, data collection, and structure determination

Purified apo enzyme was concentrated to 10 mg/mL at 4 °C using an Amicon Ultra centrifugal filter (10 kDa molecular weight cut-off; Merck, Millipore). To obtain the *At*NaMNAT in complex with NaMN, the protein was concentrated to 6–8 mg/mL and incubated with NaMN at a 50:1 molar ratio (ligand:protein) for 1 h at 4 °C prior to crystallization trials. Crystals were grown using the sitting-drop vapor-diffusion method by mixing 1 μL of protein or protein-ligand solution with 1 μL of reservoir solution and equilibrating against 100 μL of the reservoir solution. Initial screening was performed using commercial kits from JENA Bioscience. Crystals were obtained in reservoir conditions containing: 100 mM TRIS (pH 8–9), 100–200 mM $MgCl_2$, and 20–40 % (*w*/*v*) polyethylene glycol.

Crystals were mounted in MiTeGen loops and delivered to the European Molecular Biology Laboratory (EMBL), Hamburg, Germany, beamline P13 for data collection [23]. Crystallographic data analysis was carried out using MOSFLM [24] and POINTLESS [25] for initial space group determination, the XDS/XSCALE package [26] for spot integration, and AIMLESS [25] for scaling and merging. Crystals belonged to the space group $P6_522$, with typical unit-cell parameters a = b = 43 Å, c = 430 Å, and α = β = 90°, γ = 120°. Based on the protein sequence, the Matthews coefficient and solvent content calculations suggested the presence of a single molecule per asymmetric unit.

For molecular replacement, we used the in silico model AF-F4K687-F1-v4, retrieved from AlphaFold protein structure database [27]. The predicted local distance difference test (pLDDT) of 94.65 ranks the protein model in the very high confidence range. The structure was then phased by molecular replacement using Phaser [28], confirming the presence of one molecule in the asymmetric unit. Refinement of the main and side chains, ligands, and solvent molecules into electron density maps was performed using Coot [29], the Phenix suite [30], and Refmac5 [31] of the CCP4 package, under the monitoring of R_{work}, R_{free}, and the Ramachandran plot.

Interface areas were calculated with the PISA web server [32]. Fo-Fc (OMIT) and polder maps were calculated using the phenix.polder tool within the Phenix suite [30]. Table 2 reports statistics on all data collections and refinements. The X-ray crystal structures of apo *At*NaMNAT and in complex with NaMN were deposited in the Protein Data Bank with the accession codes 9RPK and 9RPM, respectively.

2.5. Site-directed mutagenesis

Site-directed mutagenesis was performed on the gene for *At*NaMNAT in the pET28a vector to generate the R106A point mutation. The mutation was introduced using the QuickChange Lightning kit (Agilent Technologies) according to the manufacturer's instructions, with primers listed in Table S1. The resulting plasmid was verified by DNA sequencing and used to transform *Escherichia coli* BL21(DE3) for protein expression and purification, following the same protocol used for the wild-type enzyme.

2.6. In silico protein structure analysis, modeling, and visualization

A structural model of *At*NaMNAT in complex with ATP ligand and a magnesium ion was built using AlphaFold3 [33], implemented in the AlphaFold server (https://alphafoldserver.com/). ATP and Mg^{2+} are included in the restricted repertoire available on the public AlphaFold server. All protein structure manipulation, analysis, and figure generation were performed using Molsoft ICM 3.9–4 software package [34]. The 3D models of *Nostoc* sp. PCC 7120 and *Gloeobacter violaceus* NaMNATs (UniProt IDs: Q8YU71 and Q7NE64, respectively) were retrieved from AlphaFold Database [27]. Complexes of these cyanobacterial NaMNATs with NaMN were generated using docking tools within MolSoft ICM.

2.7. Phylogenetic analysis

Evolutionary analysis was performed using MEGA12 software [35]. The phylogeny of 31 NaMNAT sequences, including human PNAT isoforms as outgroups, was inferred using the maximum likelihood (ML) heuristic search method with the Le-Gascuel (LG) model of amino acid substitutions [36]. The tree with the highest log likelihood is shown in Fig. 7. The initial tree used for the heuristic search was chosen based on the superior log likelihood between a neighbor-joining tree and a maximum parsimony tree.

The evolutionary rate differences among sites were modeled using a discrete gamma distribution across 5 categories (α shape parameter = 1.792), with 4 % of sites considered evolutionary invariant. Sites with data present in fewer than 95 % of the sequences were excluded using the partial deletion method.

3. Results

3.1. Biochemical characterization of Arabidopsis thaliana NaMNAT

The prevailing metabolic model for NAD biosynthesis in *A. thaliana* depicts a confluence of the de novo pathway and the Preiss–Handler salvage route, with NaMN serving as the exclusive entry point for subsequent adenylation and amidation reactions (Fig. 1) [37]. This model, however, conflicts with annotations in public protein databases (UniProt, NCBI, TAIR), which identify *Arabidopsis thaliana* NaMNAT (*At*NaMNAT) as bifunctional and suggest potential physiological activity toward both NaMN and NMN.

To elucidate the catalytic properties of *At*NaMNAT, we undertook a comprehensive kinetic analysis using purified recombinant protein

(Fig. S1A), employing both a coupled spectrophotometric assay and an HPLC-based assay, as detailed in the Methods section. First, we established optimal conditions for the enzyme assay. As shown in Fig. S1B–D, *At*NaMNAT exhibited activity across a pH range of 6.0–8.0, with robust performance at a minimal Mg^{2+} cofactor concentration of approximately 1 mM, beyond which activity plateaued. Interestingly, the enzyme from *A. thaliana*, a species adapted to temperate climates, displayed maximal activity at approximately 50 °C. This thermotolerance may confer a selective advantage during transient heat stress, which can occur in natural environments [38].

The data presented in Table 1 and Fig. S2 underscore the remarkable catalytic efficiency of *At*NaMNAT as a NaMN adenylyltransferase, as evidenced by turnover numbers of ~29 s^{-1} and ~ 27 s^{-1} and K_m values of ~24 μM and ~29 μM for NaMN and ATP, respectively. A comparative analysis of catalytic efficiencies reveals a pronounced substrate preference: *At*NaMNAT exhibits a one-thousand-fold greater efficiency for NaMN over NMN. This disparity is primarily attributable to the significantly higher K_m for NMN (~5 mM), which renders it an unlikely physiological substrate. Notably, at equimolar concentrations of NMN and NaMN (50 μM, a nearly saturating concentration for NaMN), the NMN-dependent activity was barely detectable and 666-fold lower than the NaMN adenylation activity (0.063 vs. 42.07 U/mg). Consistently, similar substrate specificities have been reported for NaMNAT enzymes of the bacterial NadD family (Table 1) [39–43]. Altogether, these kinetic data strongly suggest that NMN is unlikely to be a significant physiological substrate of the enzyme, supporting the designation of *At*NaMNAT as a canonical NaMN adenylyltransferase (EC 2.7.7.18).

Table 1
Steady-state kinetic parameters of *At*NaMNAT and the R106A mutant, compared to representative bacterial orthologs. Reported errors represent standard deviations.

Enzyme	Variable substrate	Fixed substrate	k_{cat} (s^{-1})	K_m (μM)	k_{cat}/K_m (s^{-1} mM^{-1})	Ref.
*At*NaMNAT	NaMN	ATP	26.6 ± 2.8	29.4 ± 8.1	9.05 × 10^2	This study
	ATP	NaMN	29.1 ± 1.6	24.0 ± 2.2	1.21× 10^3	This study
	NMN	ATP	6.0 ± 0.2	4616 ± 321	1.3	This study
	ATP	NMN	6.1 ± 0.6	174 ± 57	3.51× 10	This study
R106A	NaMN	ATP	3.2 ± 0.4	587 ± 87	5.45	This study
	NMN	ATP	6.78 ± 1.9	6060 ± 528	1.12	This study
*Ec*NadD	NaMN	ATP	20.7 ± 1.3	33 ± 3	6.27 × 10^2	[43]
	NMN	ATP	NR	NR	<0.6[a]	[41]
*Ba*NadD	NaMN	ATP	25.6 ± 1.2	40 ± 10	6.40 × 10^2	[18]
	NMN	ATP	0.014 ± 0.001	940 ± 120	0.015	
*Bs*NadD	NaMN	ATP	11.1 ± 1.2	43 ± 1.2	2.58 × 10^2	[39]
	NMN	ATP	0.054 ± 0.003	2300 ± 200	0.023	
*Sp*NadD	NaMN	ATP	17.4 ± 0.7	103 ± 18	1.7 × 10^2	[42]
	NMN	ATP	ND	–	–	
*Mt*NadD	NaMN	ATP	4.5 ± 0.1	340 ± 30	13.26	[40]
	NMN	ATP	0.04 ± 0.01	4000 ± 110	0.01	

NR, not reported; ND, not detected.

[a] Approximate value based on the statement that substrate preference for NaMN over NMN (calculated as k_{cat}/K_m ratio) exceeds 10^3-fold [41].

3.2. Overall structure of AtNaMNAT and comparison to other NaMNATases

The apo form of NaMNAT was crystallized in space group $P6_522$, and its structure was determined at 2.15 Å resolution and refined to final R_{work} and R_{free} values of 0.233 and 0.257, respectively (Table 2). Sequence and structural analyses of *At*NaMNAT indicate that it belongs to the large superfamily of α/β-nucleotidyltransferases possessing an N-terminal conserved dinucleotide-binding Rossmann fold [44]. This super-secondary structure (residues 19–193) consists of a highly twisted six-stranded β-sheet (β1-β6) flanked by seven α-helices (α1-α8) and connecting loops. The core β-strands adopt the topological arrangement 321456. The C-terminal domain (residues 194–238) forms the α-helices 8 and 9 (Fig. 2).

The N- and C-terminal domains possess the two highly conserved motifs, GxFxPxT/HxxH and SxT/SxxR, respectively, which are essential for ATP binding and characterize all NaMN/NMN adenylyltransferases

Table 2
Data collection and refinement statistics.

Parameter	Apoenzyme	NaMN Complex
	PDB ID: 9RPK	PDB ID: 9RPM
Wavelength (Å)	0.976	0.976
Space group	$P6_522$	$P6_522$
Cell parameters (a, b, c Å)	43.56, 43.56, 435.01	43.34, 43.34, 433.50
Resolution range (Å)	37.73–2.15 (2.23–2.15)[a]	37.54–2.66 (2.76–2.66)
Total reflections	297,304 (14322)[a]	99,126 (11721)
Unique reflections	14,722 (1408)[a]	7846 (678)
Redundancy	20 (11.5)[a]	12.4 (12.7)
Completeness (%)	99.84 (99.79)[a]	98.45 (87.93)
Mean I/σ(I)	9.6 (2.2)[a]	11.7 (1.8)
R_{merge}[b]	0.202 (0.769)[a]	0.139 (0.922)
R_{pim}[c]	0.042 (0.218)[a]	0.041 (0.535)
CC1/2	0.996 (0.889)[a]	1.00 (0.950)
CC*[d]	1.00 (0.990)	1.00 (0.987)
Reflections used in refinement	14,702 (2801)	7816 (610)
Reflections for R-free	732 (135)	383 (28)
Wilson B-factor (Å^2)	41.58	66.77
R_{work}[d]	0.233 (0.246)	0.261 (0.3164)
R_{free}[d]	0.257 (0.285)	0.305 (0.310)
Total no. of atoms[d]	1842	1809
Macromolecules	1786	1795
Ligands	0	1
Waters	52	13
Ions	4	1
Matthews coefficient (% solvent)	2.35 (47.67)	2.32 (47.07)
RMS(bonds)	0.003	0.002
RMS(angles)	0.54	0.40
Ramachandran favored (%)	94.93	97.67
Ramachandran allowed (%)	4.15	2.33
Ramachandran outliers (%)	0.92	0.00
Rotamer outliers (%)	1.46	0.48
Clashscore	3.34	5.29
Average B-factor (Å^2)		
Overall	50.91	76.74
Macromolecules	51.12	76.66
Ligands	51.69	92.19
Solvent	43.65	61.21

[a] Values in parentheses correspond to the highest-resolution shell.

[b] $R_{merge} = \frac{\sum_{hkl}\sum_j \left| I_j - \langle I \rangle \right|}{\sum_{hkl}\sum_j I_j}$, where I_j is the intensity of reflection j, and $\langle I \rangle$ is the mean intensity of all symmetry-related reflections.

[c] $R_{pim} = \frac{\sum_{hkl}\left[\frac{1}{N-1}\right]^{1/2}\sum_j \left| I_j - \langle I \rangle \right|}{\sum_{hkl}\sum_j I_j}$, where I_j is the intensity of reflection j, and $\langle I \rangle$ is the mean intensity of all symmetry-related reflections, and N is the multiplicity.

[d] Calculated using the Phenix suite. R_{free} was computed from 5 % of reflections randomly excluded from refinement.

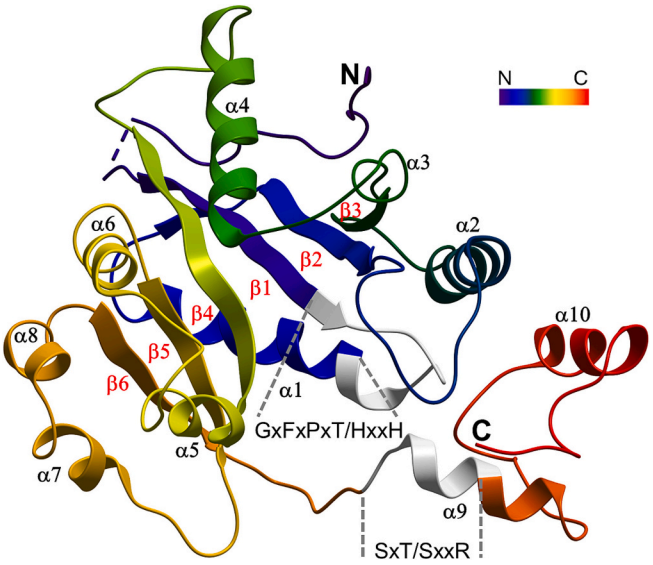

Fig. 2. Ribbon diagram of monomeric *At*NaMNAT. The protein is colored from the N-terminus (indigo) to the C-terminus (red), following an indigo–blue–green–yellow–orange gradient. Individual α-helices (α1–α10) and β-strands (β1–β6) are labeled. The N- and C-termini are marked as "N" and "C," respectively. Disordered segments are depicted with dotted traces. The GxFxPxT/HxxH and SxT/SxxR ATP-binding motifs are colored in light gray.

(Fig. 2). A structural similarity search using Dali [45] with *At*NaMNAT as the query revealed its highest structural similarity to human PNAT1 and PNAT3, as well as bacterial NadDs, with *Z*-scores in the 25–30 range (Fig. 3). *At*NaMNAT shows significantly lower structural similarity to the more divergent folds of archaeal and bacterial NadM (Z-scores 11–12) and bacterial NadR (Z-scores 10–11).

Among PNATs endowed with NaMN adenylyltransferase activity, a distinguishing feature of *At*NaMNAT (and apparently of all plant NaMNATs (Figs. 3 and S3) is a N-terminal extension (residues 1–15) connected to β1 by a disordered loop. This conserved region tethers one half of the core pleated sheet into a compact, barrel-like structure. Here, residues 1–15 make both hydrophobic and electrostatic contacts with one half of the core Rossmann fold, involving secondary elements β2, α2, β3, α3, α4 and, to a lesser extent, β1.

In detail, the main-chain carbonyls of Val3, Pro6 and Ser11 form hydrogen bonds with the side chains of Arg113 (oriented for triple stacking with Trp97 and Phe11), Tyr59 and Leu56, respectively. The Lys9 side chain extends deeply to form a hydrogen-bonding network with Ser88, Ser89 and Cys86, thereby stabilizing the α2-β3 loop. Finally, conserved Leu5 and Leu10 contribute to a compact hydrophobic core that engages helix 4 and β2β1β4 sheet (Fig. 3). As this N-terminal extension is not involved in oligomerization or substrate binding, it may contribute to protein-protein interactions or to the observed thermostability.

3.3. Subunit interactions

In agreement with gel filtration data (not shown), which suggest that *At*NaMNAT functions as a dimer, the crystal symmetry of the protein (space group $P6_522$) generates a dimeric assembly via a twofold rotation of the monomers found in the asymmetric unit (Fig. 4). A similar dimer interface geometry is observed in both eukaryotic and bacterial PNATs, despite variations in their higher-order assemblies. While bacterial NadD enzymes typically form dimers, human PNAT3 and PNAT1 assemble into tetramers and hexamers, respectively, while maintaining the core "functional dimer" structure (Fig. 4A) [39,46–48]. Recently, partial disruption of murine PNAT3 dimer interface was shown to affect protein stability and catalysis [48].

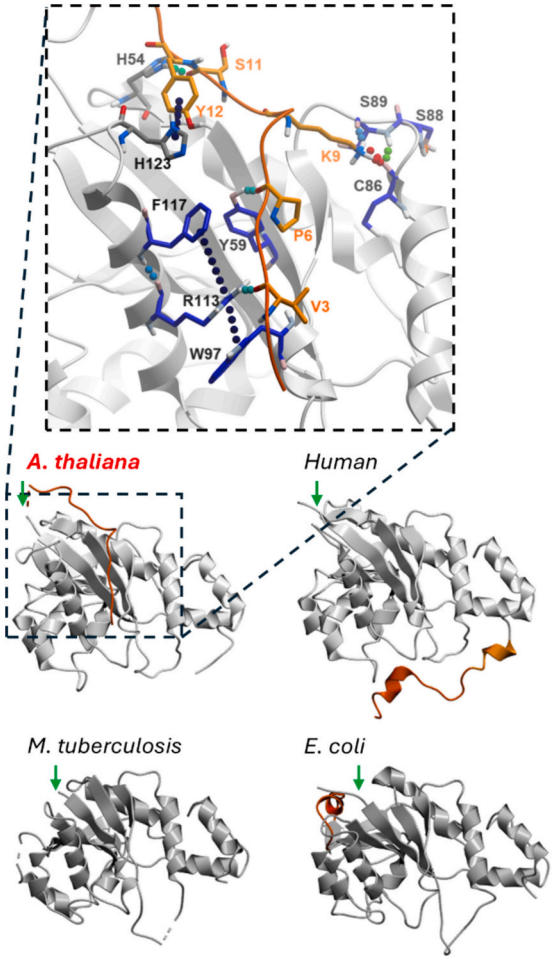

Fig. 3. Structural topology of *At*NaMNAT compared to other NaMNAT representatives. The core fold of *At*NaMNAT closely resembles that of eukaryotic PNATs and bacterial NadD family enzymes. Ribbon diagrams of human (PDB ID: 1KQO), *Mycobacterium tuberculosis* (PDB ID: 4X0E), and *Escherichia coli* (PDB: 1K4K) NaMNATs highlight the conserved overall topology across species. The top panel shows a close-up view of the *At*NaMNAT N-terminal region, with colored dotted lines indicating hydrogen bonds and black dotted lines showing π–π or cation–π interactions (distance F117–W97 is 9.6 Å). Residues participating in these interactions are shown as sticks.

The dimer interface encompasses a total buried surface area of approximately 1109 $Å^2$ per monomer, primarily involving the C-terminal domains and, to a lesser extent, the α1 helix (Fig. 4B). The dimerization interface of *At*NaMNAT is identical in its apo- and NaMN-complexed forms, with no evident conformational changes. The interface is stabilized by an array of hydrogen bonds and hydrophobic interactions between α-helix 1, the loop between α-helix 2 and β-strand 3, and the C-terminal domain encompassing α-helices 9 and 10.

Specifically, the aromatic ring of Phe35 from one monomer stacks with Phe35 from the other monomer (Fig. 4B), while Tyr218 interacts with Leu38 from the opposing monomer (not shown for clarity). Val197 contributes to a hydrophobic patch by engaging interactions with Ile201, Leu206, Leu219 and Arg205 from the adjacent subunit. Ser215 is the major contributor to intersubunit electrostatic stabilization, forming three strong hydrogen bonds with the side chains of Glu42 and Asp46 and with the main-chain carbonyl of Arg39. Additional hydrogen bonds between Lys 217 and Ser88, and between Arg205 and Thr196, further reinforce the dimer interface (Fig. 4B).

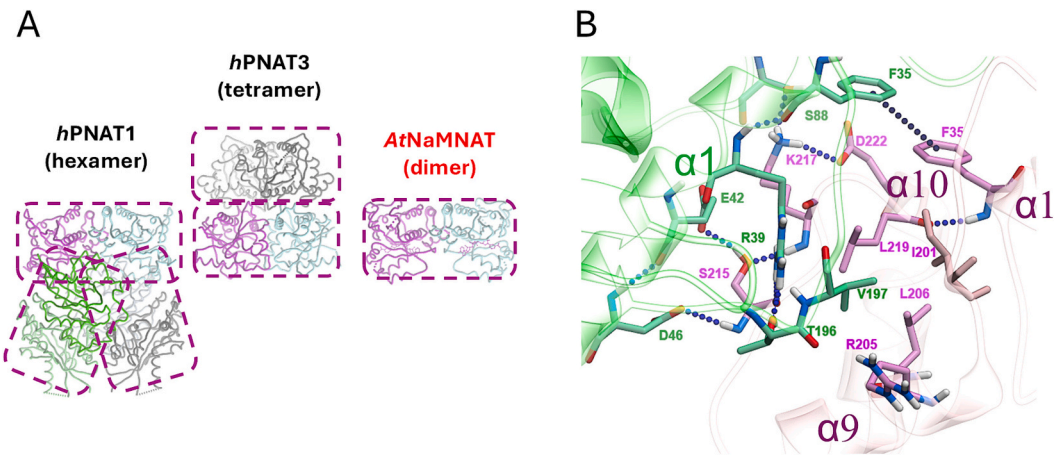

Fig. 4. (A) Different oligomeric assemblies of NaMNATs illustrating the conserved dimeric protomer. Crystal structure of *A. thaliana* NaMNAT (*At*NaMNAT, dimer) is shown alongside human PNAT1 (*h*PNAT1, hexamer) and human PNAT3 (*h*PNAT3, tetramer). Purple dashed boxes highlight the core dimeric unit of quaternary structures. (B) Structural details of the *At*NaMNAT dimer interface. Key residues mediating dimer assembly and stability are highlighted in stick representation. Additional interactions are described in the text. Subunits A and B are colored green and pink, respectively. For clarity, the symmetrical portion of the interface—mirrored across the F35–F35 π–π interaction—is omitted.

3.4. The NaMN binding site

The crystal structure of *At*NaMNAT bound with the substrate NaMN (Fig. S4) was determined to investigate protein-ligand interactions, conformational changes upon substrate binding, and the structural basis for substrate specificity. The *At*NaMNAT–NaMN complex crystallized in space group $P6_522$, and the structure was determined to a resolution of 2.66 Å (Table 2). The model was refined to final R_{work} and R_{free} values of 0.261 and 0.305, respectively. A detailed examination of the active site region, supported by a structure-based sequence alignment of representative PNATs with exclusive NaMN adenylyltransferase activity, revealed both conserved and divergent structural features (Figs. 5 and 6). *At*NaMNAT binds the NaMN substrate via an extensive network of hydrogen bonds, π-stacking effects, salt bridges and dipole interactions (Fig. 6A). The phosphate group of NaMN is hydrogen-bonded with the side chain and main-chain amide of Ser29. The ribose O2' and O3' atoms form hydrogen bonds to the side chain of Tyr104, while the 2'-OH hydrogen interacts with the highly conserved Glu98. The pyridine ring of the nicotinate moiety engages in a strictly conserved stacking interaction with the indole ring of Trp149. The carboxylic acid group is stabilized by two direct hydrogen bonds between the O8 atom and both the side chain and backbone amide of Thr107.

These interactions with NaMN, or the NaMN portion of NaAD, are consistently observed in the structures of bacterial NaMNAT enzymes and in more divergent human PNATs. This conservation, independent of substrate preference, underscores the crucial role of these residues (Fig. 5) in stabilizing the pyridine ring and carbonyl group common to both NaMN and NMN.

Additional residues determine NaMN versus NMN specificity; in the bacterial NadD family, NaMN specificity is ensured by a second hydrogen bond between the carboxylate O7 atom and the main-chain amide of a tyrosine residue (e.g., Tyr117 in *B. anthracis* and Tyr118 in *E. coli*, Fig. 6B). This anion-binding pocket is stabilized by π–π stacking between the same tyrosine and another conserved tyrosine (Tyr84 in both *B. anthracis* and *E. coli*). By contrast, in *At*NaMNAT, the negative charge of the nicotinosyl moiety is neutralized by the positively charged guanidinium group of Arg106, which forms hydrogen bonds with both the nicotinate and the backbone carbonyl of Val148. A focused structure-based multiple sequence alignment of NaMNATs from photosynthetic organisms reveals that Arg106 is highly conserved across plants, algae, and cyanobacteria, suggesting a critical role in substrate discrimination (Fig. S3). This distinctive structural feature appears to be a hallmark of NaMNAT enzymes in photoautotrophs.

Upon NaMN binding, loop 146–151 moves closer to the active site, driven by the interaction of Trp149 with the ligand and by Arg106 bridging the main chain carbonyl of Val148 and the nicotinate moiety. Superposition of the apo-enzyme and the NaMN-bound complex also shows that, in the apo conformation, Arg106 is collapsed inward, forming a π–cation bond with Trp149 (Fig. 6C). In this state, Arg106 would sterically clash with the nicotinosyl moiety, thus preventing proper substrate binding. Thr107 also reorients upon substrate engagement, repositioning Arg106 into its catalytically competent conformation (Fig. 6C).

3.5. Functional characterization of Arg106 mutant

The functional importance of Arg106 in NaMNAT activity was further investigated through site-directed mutagenesis and kinetic analysis. An R106A mutant was generated, and its kinetic parameters for NaMN and NMN were determined at saturating ATP concentrations (Table 1). Whereas the k_{cat} and K_m values for NMN were unaffected, both the affinity for NaMN and the maximal catalytic rate decreased by approximately 20- and 8-fold, respectively, resulting in an overall 166-fold reduction in catalytic efficiency. These findings confirm the critical role of Arg106 in substrate recognition and catalysis.

The pronounced effect on K_m suggests that Arg106 primarily contributes to stabilizing substrate binding rather than significantly altering the catalytic geometry. This residue likely facilitates neutralization of the nicotinate carboxylate, thereby promoting productive alignment of NaMN in the active site. Collectively, our structural and sequence analyses indicate that Arg106 is an invariant residue among NaMNATs from photosynthetic organisms, where it plays a central role in NaMN recognition and catalysis.

3.6. The ATP binding site

Because we were unable to determine a crystal structure of *At*NaMNAT complexed with either the ATP substrate or the NaAD product at sufficient resolution, we employed the most recent iteration of AlphaFold (AlphaFold 3) to generate a predictive model of *At*NaMNAT bound to ATP and a magnesium ion (predicted template modeling score, pTM = 0.93) (Fig. 6D). In this monomer–ligand model, the interface predicted template modeling score, ipTM of 0.95, indicates a highly reliable binding pose and favorable interaction geometry. The ATP molecule, together with its associated Mg^{2+} ion, occupies the predicted active site located within a deep cleft between the β1 and β4 strands at the

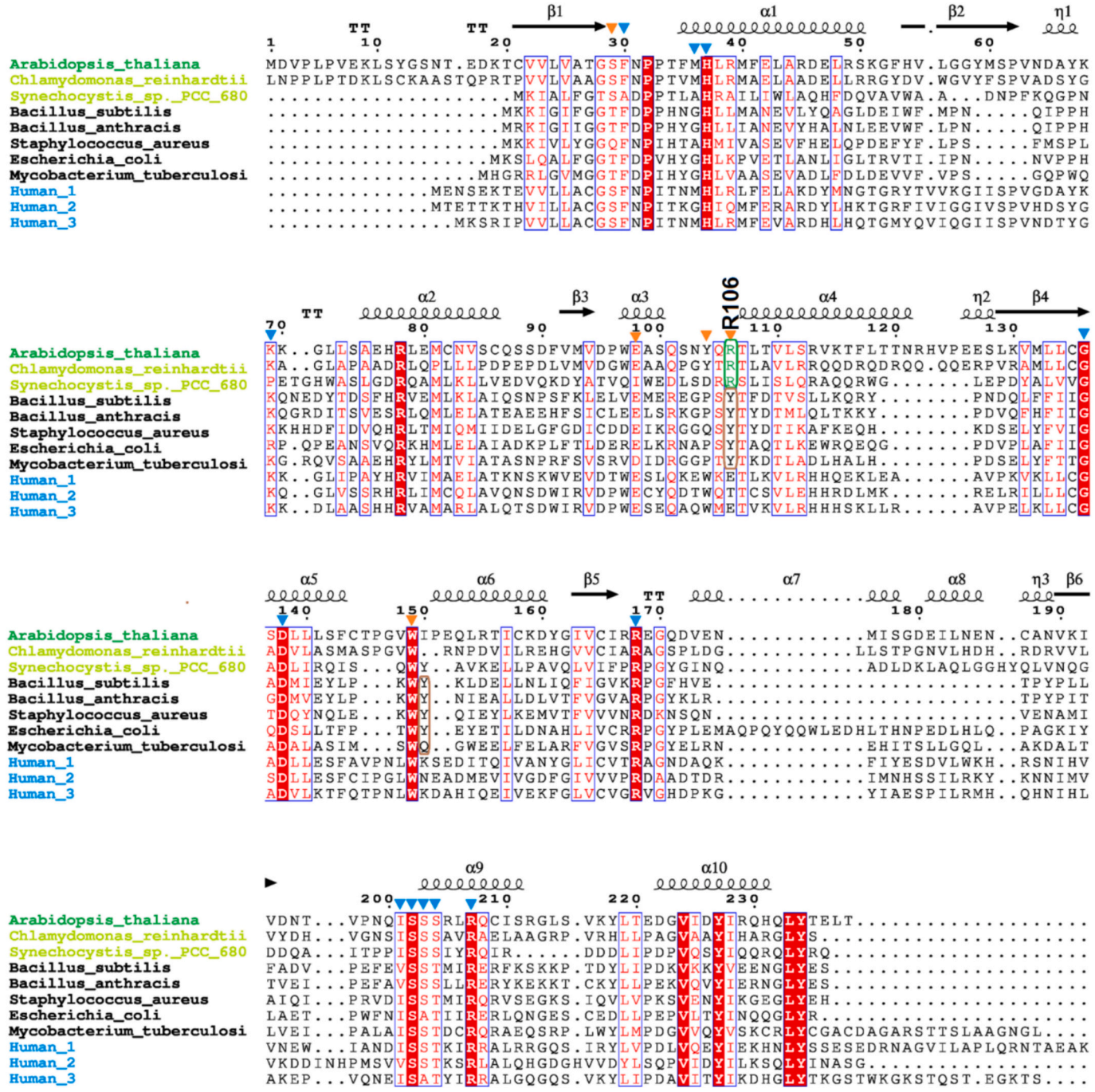

Fig. 5. Structure-based sequence alignment of NaMNATs from bacterial and eukaryotic sources. Photosynthetic organisms (a plant, an alga, and a cyanobacterium) are highlighted in green, bacteria are in black, and humans in blue. Residue numbering and secondary structure elements correspond to the *A. thaliana* NaMNAT structure. Critical residues involved in NaMN and ATP binding are indicated with orange and blue arrows, respectively. Conserved residues are boxed, and those that are invariably conserved have a red background. The two co-evolved tyrosines conferring bacterial-like NaMN substrate specificity are circled in brown, while the key arginines responsible for NaMN specificity in photosynthetic organisms are circled in green. Fig. S3 provides an expanded view of the NaMNAT family from photosynthetic organisms, including additional land plants, cyanobacteria, and algae.

α/β-sheet topological switch point. The ATP adopts a characteristic bend at the α–β phosphate bond, facilitating nucleophilic attack by the 5′-phosphate of NaMN.

Inspection of residues stabilizing ATP in the model revealed strong conservation of this region with other NMN/NaMN adenylyltransferases [12,47]. As expected, residues known to interact with ATP across the PNAT family also engage the substrate in *At*NaMNAT. These residues form part of the classic ATP-binding fingerprint motifs GxFxPxT/HxxH and SxT/SxxR, as well as the mobile loops β2-α2 and β5-α7 [49,50]. These loops move inward to interact with the terminal γ-phosphate and adenine ring of ATP, respectively (Fig. 6D). The adenine ring of ATP is sandwiched between Arg168, which stacks against the adenine with its guanidinium group, and Met36. Notably, Met36 is oriented inward in the apo structure; upon ATP binding, it rotates outward to accommodate the adenosine moiety (Fig. 6D). The carbonyl oxygen of Ile201 further interacts with the adenine N6 atom, while the ribose hydroxyl groups are hydrogen-bonded with Asp138 and Gly136, which are invariably conserved in the NaMNAT family (Fig. 5). The bending of the α–β

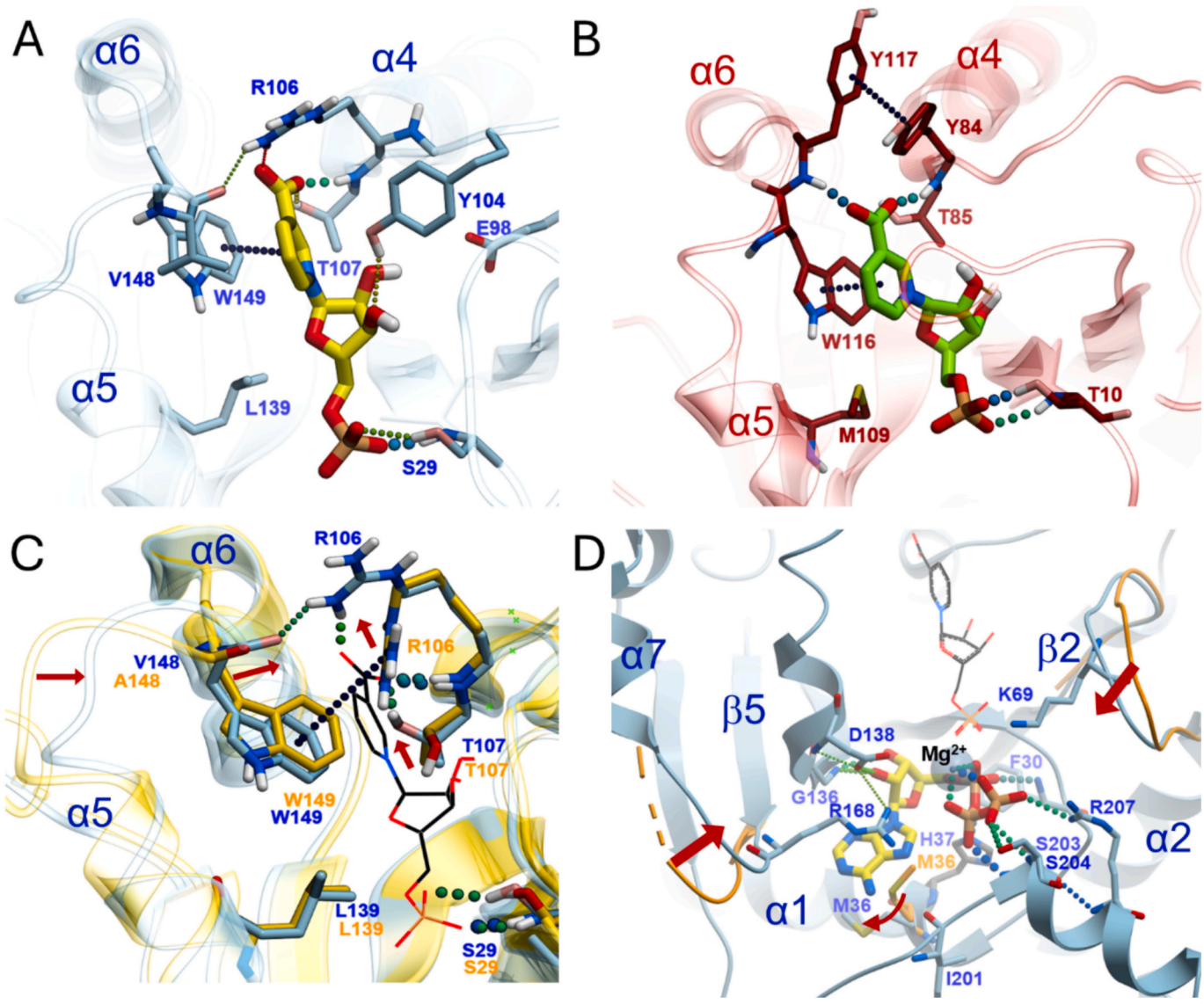

Fig. 6. (A–D) NaMN and ATP binding sites. (A) Close-up view of *A. thaliana* NaMNAT in complex with NaMN. Binding residues in direct contact with the ligand (through hydrogen-bonds or π–interactions) are shown as sticks. (B) Close-up view of *B. anthracis* NadD in complex with NaMN (PDB ID: 3E27). (C) Superposition between *At*NaMNAT in the free (yellow ribbon) and substrate-bound (cyan) form. Red arrows point out conformational changes upon ligand-binding. (D) Superposition of *At*NaMNAT in the free and predicted *At*NaMNAT-ATP complex forms. For clarity, only the β2α2 and β5α7 loops and Met36 side chain of the free protein (orange), which undergo significant movement upon ligand binding, are shown. The position of NaMN substrate, modeled from the NaMN-bound complex, is shown in wire representation. Magnesium ion is shown in CPK representation.

phosphate bond is stabilized by two salt bridges between the β- and γ-phosphates and Lys69 and Arg207, and by strong hydrogen bonds involving the main chain amides of Ser203 and Ser204. Finally, the α-phosphate group is stabilized through hydrogen bonds with the NE2 atom of His37 and the main-chain nitrogen of Phe30.

Comparisons of the apo-*At*NaMNAT, NaMN- and ATP-bound forms of *At*NaMNAT reveals moderate conformational changes overall (Fig. 6C–D), consistent with substrate affinities in the low-micromolar range and with the apoenzyme adopting a conformation that readily accommodates both substrates.

3.7. Evolutionary insights into the origin of plant NaMN-specific PNAT

Our sequence and structural analyses reveal that substrate specificity for NaMN versus NMN in photosynthetic eukaryotes hinges on a key positively charged arginine residue that counteracts the nicotinate anion (Figs. 5 and 6A). In contrast, the anion-binding pocket of bacterial NadD features two main-chain amides that interact with the nicotinate carboxylate oxygens through a conserved π–π stacking network (Fig. 6B). Strikingly, both types of NaMN-binding pockets appear to coexist among cyanobacterial NadD homologs.

A multiple sequence alignment of 13 cyanobacterial PNATs with confirmed NaMNAT specificity—either experimentally determined or inferred by genomic reconstruction [51]—reveals a distinct division: approximately half of the species contain a conserved arginine equivalent to *At*NaMNAT Arg106, while the other half possess two aromatic residues equivalent to *E. coli* NadD Tyr118 and Tyr184 (Fig. S3).

This observation provides valuable insights into the evolutionary path that led to the NaMN-specific PNATs in both photosynthetic eukaryotes and bacteria. Consistently, a phylogenetic analysis of NaMNAT sequences shows that these two cyanobacterial groups form well-separated clades (Fig. 7). One branch, closer to bacterial sequences and including members of the *Prochlorococcus* genus, carries the "bacterial-type" NaMN specificity mechanism (labeled "NH"). The second

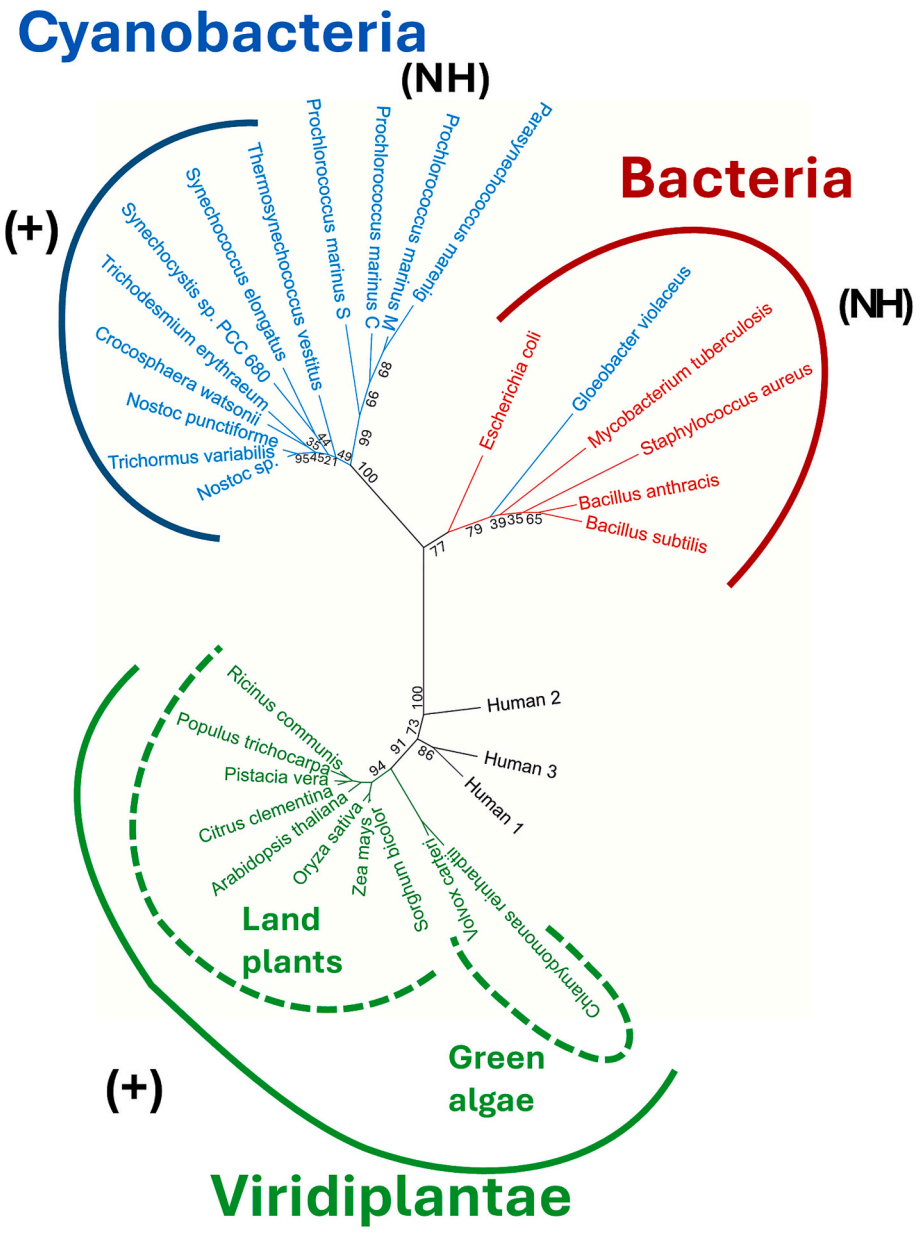

Fig. 7. Phylogenetic analysis of representative NaMNATs enriched with photosynthetic organisms. The tree reveals three distinct clades representing Cyanobacteria (blue), Bacteria (red), and Viridiplantae (green), with human sequences (black) forming their own divergent group as representatives of bifunctional NaMN/NMN-ATs. The percentage of replicate trees ($n = 109$, determined adaptively [35]) in which the associated taxa formed a cluster is shown below the branches. The (+) and (NH) labels indicate NaMNAT groups employing distinct strategies to ensure strict NaMN substrate specificity.

clade, which includes the experimentally characterized NadD from *Synechocystis* sp. PCC 680 (locus sll1916) [51], exhibits the "Viridiplantae-type" NaMN-specificity mechanism (labeled "+").

Based on the branching pattern, an ancient horizontal gene transfer (HGT) event likely occurred from *Gloebacter*-like cyanobacteria to a bacterial lineage, introducing a distinct strategy for NaMN recognition that was subsequently retained in bacterial taxa. This interpretation is consistent with the basal phylogenetic position of *Gloeobacter violaceus* within cyanobacteria, as Gloeobacter represents one of the earliest-diverging cyanobacterial lineages [52]. In parallel, the maximum-likelihood tree indicates that Viridiplantae probably acquired a related but distinct version of NaMNAT from the cyanobacterial endosymbiont that gave rise to chloroplasts. Notably, the "+" clade includes representatives of N_2-fixing Chrococcales and filamentous Nostocales, which are regarded as the cyanobacterial taxa most closely related to the plastid ancestor [53].

Three-dimensional models of NaMNAT in complex with NaMN from representative cyanobacterial species of the "NH" and "+" groups (Fig. S5) recapitulate the active-site architectures experimentally resolved for *At*NaMNAT and bacterial NaMNAT (Fig. 6A–B). These findings indicate that plant- and bacterial-type strategies for ensuring NaMN substrate specificity likely emerged in ancient cyanobacteria. Collectively, the results support a complex evolutionary origin of NaMNATs in bacteria and plants, shaped by multiple contributions from cyanobacterial lineages.

4. Discussion

NAD is a fundamental coenzyme found in all living cells, serving dual roles as a redox mediator in metabolism and as a signaling molecule. In plants, NAD metabolism exhibits unique features tightly integrated with photosynthesis, organellar compartmentalization, and specialized

defense signaling networks [54]. Cellular NAD levels fluctuate markedly in response to environmental stressors such as drought, heat, salinity, and pathogen attacks, often leading to energy depletion and oxidative damage [55,56]. Consequently, engineering NAD metabolism has emerged as a promising biotechnological strategy: boosting its biosynthesis, recycling, or availability can improve plant resilience, supporting growth and yield under adverse conditions. Thus, NAD metabolism represents a key target for optimizing plant stress responses and development [57].

Despite its central role, major gaps remain in our understanding of plant NAD metabolism, particularly regarding the structural and mechanistic characterization of NAD biosynthetic enzymes. In this work, we focused on the central NAD biosynthesis enzyme PNAT from *A. thaliana*. In all living organisms, the PNAT family of enzymes catalyzes the only reaction common to both de novo and salvage/recycling routes leading to NAD formation, i.e., the ATP-dependent adenylation of NMN or NaMN to NAD or NaAD, respectively. Members of the PNAT family differ in substrate specificity, depending on the organism. Some are bifunctional, acting with equivalent activity on both NMN and NaMN (e.g., archaeal NadM and mammalian PNAT isoforms), whereas others exhibit strict substrate selectivity. For instance, bacterial NadR is NMN-specific, while NadD exclusively processes NaMN.

The first reported characterization of a plant PNAT in 2007 described a recombinant glutathione S-transferase (GST)-tagged *A. thaliana* enzyme with apparently similar efficiencies toward NaMN and NMN adenylation [11]. Accordingly, the enzyme remains annotated in databases as a bifunctional NMN/NaMN adenylyltransferase. However, this classification contrasts with comparative genomic analyses indicating that in plants, NAD is preferentially synthesized via the deamidated pathway [15,37]. Metabolic tracing in *Coffea arabica* also supports this view, showing that NMN is more likely a degradation product of NAD rather than an intermediate in NAD biosynthesis [58]. Indeed, NMN can arise through the activity of Nudix hydrolases that cleave the pyrophosphate bond of free NAD or NAD-capped RNA in vitro [59,60].

Our kinetic characterization of *A. thaliana* PNAT, integrated with genomic and structural analyses, reveals a strict specificity for NaMN over NMN, confirming that NAD biosynthesis in plants proceeds predominantly through the deamidated pathway. The discrepancy between our findings and those reported for the GST-tagged enzyme likely reflects the influence of the large GST tag, which can alter protein structure, oligomerization and catalytic properties [61,62]. Moreover, the previous study lacked a detailed experimental description of the NaMN adenylyltransferase assay [11].

NAD metabolomic profiling in *A. thaliana* tissues further supports this interpretation. NMN levels are consistently several hundred times higher than those of NaMN, mirroring the approximately 300-fold difference between the K_m values for NMN (~5 mM) and NaMN (~0.02 mM) [63]. This strong correlation further supports our finding that NaMN is the true physiological substrate of *At*NaMNAT. Furthermore, the maximal NAD concentration in subcellular compartments (~1.5 mM) is substantially lower than the K_m for NMN [64], making it unlikely that *At*NaMNAT participates in NMN recycling from Nudix-mediated NAD degradation.

Other, yet unidentified, enzymes may regulate NMN turnover instead. Interestingly, our search for remote NaMNAT homologs in *A. thaliana* identified two uncharacterized paralogs (UniProt IDs: Q8L845 and Q84Q59, 89 % identical) encoded by *At2g01220* and *At3g27610* genes. Each protein contains an N-terminal domain homologous to the bacterial NMN deamidase PncC and a C-terminal domain belonging to the nucleotidyltransferase superfamily. Remarkably, the PncC fold has not been previously described outside the bacterial kingdom [65,66]. Structural prediction using FFAS03 [67] and Dali confirmed this domain assignment (Tables S2–3 and Fig. S6). If future kinetic studies validate their NMN deamidase activity, these proteins could represent a novel plant-specific mechanism for converting NMN to NaMN, effectively linking NMN recycling to the Preiss–Handler pathway (Fig. 1).

The strict NaMN specificity of the *A. thaliana* enzyme represents the first case reported in eukaryotes and only the second example after the bacterial NadD. Sequence clustering suggests that this specificity extends across green plants and algae. The deamidated routes to NAD—initiated from Na, Qa, or Nam—require three energetically demanding steps, whereas the amidated pathway converting Nam directly to NAD via NMN involves only two ATP-dependent reactions. Despite this apparent energetic disadvantage, the deamidated route predominates in bacteria, yeast, and plants [68]. Interestingly, phylogenetic surveys indicate that nicotinamidase, a key enzyme in the deamidated pathway, is enriched in extremophilic bacteria, possibly due to the greater thermal stability of deamidated intermediates compared to amidated ones [68]. This stability advantage may also explain the prevalence of the deamidated pathway in plants.

High-resolution crystal structures of *At*NaMNAT in its apo and NaMN-bound forms provide further clarification of the structural basis for NaMN specificity. These are the first PNAT structures from a plant source, filling a critical gap in our understanding of plant NAD metabolism. To date, no crystal structures have been reported for other major plant NAD-related enzymes (Fig. 1). Therefore, future efforts to advance our understanding of plant NAD biology should prioritize three-dimensional structural analyses of these enzymes.

CRediT authorship contribution statement

Leonardo Sorci: Writing – review & editing, Writing – original draft, Visualization, Software, Resources, Investigation, Funding acquisition, Formal analysis, Data curation, Conceptualization. **Michele Cianci:** Writing – review & editing, Software, Resources, Investigation, Formal analysis, Data curation. **Carlo Fortunato:** Investigation, Formal analysis, Data curation. **Massimiliano Gasparrini:** Writing – review & editing, Validation, Methodology. **Nadia Raffaelli:** Writing – review & editing, Supervision, Resources, Project administration, Investigation, Funding acquisition.

Declaration of competing interest

The authors declare that they have no known competing financial interests or personal relationships that could have appeared to influence the work reported in this paper.

Acknowledgments

This work was supported by Marche Polytechnic University RSA2023 grants to LS, MC and NR. X-ray diffraction data were collected at the PETRA III storage ring operated by EMBL Hamburg (DESY, Hamburg, Germany; beam time award number MX-848). We thank the facility for the allocated beam time and technical support.

Appendix A. Supplementary data

Supplementary data to this article can be found online at https://doi.org/10.1016/j.ijbiomac.2025.148370.

Data availability

Data will be made available on request.

References

[1] G. Noctor, J. Hager, S. Li, Biosynthesis of NAD and its manipulation in plants, in: F. Rébeillé, R. Douce (Eds.), Advances in Botanical Research, Academic Press, Oxford, 2011, pp. 153–201, https://doi.org/10.1016/B978-0-12-386479-6.00002-0.

[2] B. Gakière, J. Hao, L. de Bont, P. Pétriacq, A. Nunes-Nesi, A.R. Fernie, NAD+ biosynthesis and signaling in plants, Crit. Rev. Plant Sci. 37 (4) (2018) 259–307, https://doi.org/10.1080/07352689.2018.1505591.
[3] G. Noctor, G. Queval, B. Gakiere, NAD(P) synthesis and pyridine nucleotide cycling in plants and their potential importance in stress conditions, J. Exp. Bot. 57 (8) (2006) 1603–1620, https://doi.org/10.1093/jxb/erj202.
[4] S. Gerdes, C. Lerma-Ortiz, O. Frelin, S.M. Seaver, C.S. Henry, V. de Crecy-Lagard, A. D. Hanson, Plant B vitamin pathways and their compartmentation: a guide for the perplexed, J. Exp. Bot. 63 (15) (2012) 5379–5395, https://doi.org/10.1093/jxb/ers208.
[5] A. Katoh, K. Uenohara, M. Akita, T. Hashimoto, Early steps in the biosynthesis of NAD in Arabidopsis start with aspartate and occur in the plastid, Plant Physiol. 141 (3) (2006) 851–857, https://doi.org/10.1104/pp.106.081091.
[6] L. Hunt, M.J. Holdsworth, J.E. Gray, Nicotinamidase activity is important for germination, Plant J. 51 (3) (2007) 341–351, https://doi.org/10.1111/j.1365-313X.2007.03151.x.
[7] G. Wang, E. Pichersky, Nicotinamidase participates in the salvage pathway of NAD biosynthesis in Arabidopsis, Plant J. 49 (6) (2007) 1020–1029, https://doi.org/10.1111/j.1365-313X.2006.03013.x.
[8] L. Jeanguenin, A. Lara-Nunez, D.A. Rodionov, A.L. Osterman, N.Y. Komarova, D. Rentsch, J.F. Gregory 3rd, A.D. Hanson, Comparative genomics and functional analysis of the NiaP family uncover nicotinate transporters from bacteria, plants, and mammals, Funct. Integr. Genomics 12 (1) (2012) 25–34, https://doi.org/10.1007/s10142-011-0255-y.
[9] J.H.M. Schippers, A. Nunes-Nesi, R. Apetrei, J. Hille, A.R. Fernie, P.P. Dijkwel, The Arabidopsis onset of leaf death5 mutation of quinolinate synthase affects nicotinamide adenine dinucleotide biosynthesis and causes early ageing, Plant Cell 20 (10) (2008) 2909–2925, https://doi.org/10.1105/tpc.107.056341.
[10] L. Wu, D. Ren, S. Hu, G. Li, G. Dong, L. Jiang, X. Hu, W. Ye, Y. Cui, L. Zhu, J. Hu, G. Zhang, Z. Gao, D. Zeng, Q. Qian, L. Guo, Down-regulation of a nicotinate phosphoribosyltransferase gene, OsNaPRT1, leads to withered leaf tips, Plant Physiol. 171 (2) (2016) 1085–1098, https://doi.org/10.1104/pp.15.01898.
[11] S.-n. Hashida, H. Takahashi, M. Kawai-Yamada, H. Uchimiya, *Arabidopsis thaliana* nicotinate/nicotinamide mononucleotide adenyltransferase (AtNMNAT) is required for pollen tube growth, Plant J. 49 (4) (2007) 694–703, https://doi.org/10.1111/j.1365-313X.2006.02989.x.
[12] C. Lau, M. Niere, M. Ziegler, The NMN/NaMN adenylyltransferase (NMNAT) protein family, Front. Biosci. 14 (2) (2009) 410–431, https://doi.org/10.2741/3252.
[13] X. Zhang, O.V. Kurnasov, S. Karthikeyan, N.V. Grishin, A.L. Osterman, H. Zhang, Structural characterization of a human cytosolic NMN/NaMN Adenylyltransferase and implication in human NAD biosynthesis, J. Biol. Chem. 278 (15) (2003) 13503–13511, https://doi.org/10.1074/jbc.M300073200.
[14] P. Franchetti, R. Petrelli, L. Cappellacci, M. Pasqualini, P. Vita, L. Sorci, F. Mazzola, N. Raffaelli, G. Magni, Synthesis and biological evaluation of NAD analogs as human pyridine nucleotide adenylyltransferase inhibitors, Nucleos. Nucleot. Nucl. 24 (5–7) (2005) 477–479, https://doi.org/10.1081/NCN-200060013.
[15] L. Sorci, O. Kurnasov, D.A. Rodionov, A.L. Osterman, Genomics and enzymology of NAD biosynthesis, in: H.-W. Liu, L. Mander (Eds.), Comprehensive Natural Products II, Elsevier, Oxford, 2010, pp. 213–257, https://doi.org/10.1016/B978-008045382-8.00138-6.
[16] N. Huang, L. Sorci, X. Zhang, C.A. Brautigam, X. Li, N. Raffaelli, G. Magni, N. V. Grishin, A.L. Osterman, H. Zhang, Bifunctional NMN adenylyltransferase/ADP-ribose pyrophosphatase: structure and function in bacterial NAD metabolism, Structure 16 (2) (2008) 196–209, https://doi.org/10.1016/j.str.2007.11.017.
[17] L. Sorci, I. Blaby, J. De Ingeniis, S. Gerdes, N. Raffaelli, V. de Crécy Lagard, A. Osterman, Genomics-driven reconstruction of acinetobacter NAD metabolism: insights for antibacterial target selection, J. Biol. Chem. 285 (50) (2010) 39490–39499, https://doi.org/10.1074/jbc.M110.185629.
[18] L. Sorci, D. Martynowski, D.A. Rodionov, Y. Eyobo, X. Zogaj, K.E. Klose, E. V. Nikolaev, G. Magni, H. Zhang, A.L. Osterman, Nicotinamide mononucleotide synthetase is the key enzyme for an alternative route of NAD biosynthesis in Francisella tularensis, Proc. Natl. Acad. Sci. USA 106 (9) (2009) 3083–3088, https://doi.org/10.1073/pnas.0811718106.
[19] S.K. Singh, O.V. Kurnasov, B. Chen, H. Robinson, N.V. Grishin, A.L. Osterman, H. Zhang, Crystal structure of *Haemophilus influenzae* NadR protein. A bifunctional enzyme endowed with NMN adenylyltransferase and ribosylnicotinamide kinase activities, J. Biol. Chem. 277 (36) (2002) 33291–33299, https://doi.org/10.1074/jbc.M204368200.
[20] J.L. Brunelle, R. Green, One-dimensional SDS-polyacrylamide gel electrophoresis (1D SDS-PAGE), in: J. Lorsch (Ed.), Methods in Enzymology, Academic Press, Oxford, 2014, pp. 151–159, https://doi.org/10.1016/B978-0-12-420119-4.00012-4.
[21] M.M. Bradford, A rapid and sensitive method for the quantitation of microgram quantities of protein utilizing the principle of protein-dye binding, Anal. Biochem. 72 (1) (1976) 248–254, https://doi.org/10.1016/0003-2697(76)90527-3.
[22] V. Mori, A. Amici, F. Mazzola, M. Di Stefano, L. Conforti, G. Magni, S. Ruggieri, N. Raffaelli, G. Orsomando, Metabolic profiling of alternative NAD biosynthetic routes in mouse tissues, PLoS One 9 (11) (2014) e113939, https://doi.org/10.1371/journal.pone.0113939.
[23] M. Cianci, G. Bourenkov, G. Pompidor, I. Karpics, J. Kallio, I. Bento, M. Roessle, F. Cipriani, S. Fiedler, T.R. Schneider, P13, the EMBL macromolecular crystallography beamline at the low-emittance PETRA III ring for high- and low-energy phasing with variable beam focusing, J. Synchrotron Radiat. 24 (1) (2017) 323–332, https://doi.org/10.1107/S1600577516016465.
[24] T.G.G. Battye, L. Kontogiannis, O. Johnson, H.R. Powell, A.G.W. Leslie, iMOSFLM: a new graphical interface for diffraction-image processing with MOSFLM, Acta Crystallogr. D 67 (4) (2011) 271–281, https://doi.org/10.1107/S0907444910048675.
[25] P.R. Evans, An introduction to data reduction: space-group determination, scaling and intensity statistics, Acta Crystallogr. D 67 (Pt 4) (2011) 282–292, https://doi.org/10.1107/s090744491003982x.
[26] W. Kabsch, XDS, Acta Crystallogr. D 66 (2) (2010) 125–132, https://doi.org/10.1107/S0907444909047337.
[27] M. Varadi, S. Anyango, M. Deshpande, S. Nair, C. Natassia, G. Yordanova, D. Yuan, O. Stroe, G. Wood, A. Laydon, A. Žídek, T. Green, K. Tunyasuvunakool, S. Petersen, J. Jumper, E. Clancy, R. Green, A. Vora, M. Lutfi, M. Figurnov, A. Cowie, N. Hobbs, P. Kohli, G. Kleywegt, E. Birney, D. Hassabis, S. Velankar, Alphafold protein structure database: massively expanding the structural coverage of protein-sequence space with high-accuracy models, Nucleic Acids Res. 50 (D1) (2021) D439–D444, https://doi.org/10.1093/nar/gkab1061.
[28] A.J. McCoy, R.W. Grosse-Kunstleve, P.D. Adams, M.D. Winn, L.C. Storoni, R. J. Read, Phaser crystallographic software, J. Appl. Crystallogr. 40 (4) (2007) 658–674, https://doi.org/10.1107/S0021889807021206.
[29] P. Emsley, K. Cowtan, Coot: model-building tools for molecular graphics, Acta Crystallogr. D 60 (12 Part 1) (2004) 2126–2132, https://doi.org/10.1107/S0907444904019158.
[30] D. Liebschner, P.V. Afonine, M.L. Baker, G. Bunkoczi, V.B. Chen, T.I. Croll, B. Hintze, L.-W. Hung, S. Jain, A.J. McCoy, N.W. Moriarty, R.D. Oeffner, B.K. Poon, M.G. Prisant, R.J. Read, J.S. Richardson, D.C. Richardson, M.D. Sammito, O. V. Sobolev, D.H. Stockwell, T.C. Terwilliger, A.G. Urzhumtsev, L.L. Videau, C. J. Williams, P.D. Adams, Macromolecular structure determination using X-rays, neutrons and electrons: recent developments in Phenix, Acta Crystallogr. D 75 (10) (2019) 861–877, https://doi.org/10.1107/S2059798319011471.
[31] G.N. Murshudov, A.A. Vagin, E.J. Dodson, Refinement of macromolecular structures by the maximum-likelihood method, Acta Crystallogr. D 53 (3) (1997) 240–255, https://doi.org/10.1107/S0907444996012255.
[32] E. Krissinel, K. Henrick, Inference of macromolecular assemblies from crystalline state, J. Mol. Biol. 372 (3) (2007) 774–797, https://doi.org/10.1016/j.jmb.2007.05.022.
[33] J. Abramson, J. Adler, J. Dunger, R. Evans, T. Green, A. Pritzel, O. Ronneberger, L. Willmore, A.J. Ballard, J. Bambrick, S.W. Bodenstein, D.A. Evans, C.-C. Hung, M. O'Neill, D. Reiman, K. Tunyasuvunakool, Z. Wu, A. Žemgulytė, E. Arvaniti, C. Beattie, O. Bertolli, A. Bridgland, A. Cherepanov, M. Congreve, A.I. Cowen-Rivers, A. Cowie, M. Figurnov, F.B. Fuchs, H. Gladman, R. Jain, Y.A. Khan, C.M. R. Low, K. Perlin, A. Potapenko, P. Savy, S. Singh, A. Stecula, A. Thillaisundaram, C. Tong, S. Yakneen, E.D. Zhong, M. Zielinski, A. Žídek, V. Bapst, P. Kohli, M. Jaderberg, D. Hassabis, J.M. Jumper, Accurate structure prediction of biomolecular interactions with AlphaFold 3, Nature 630 (8016) (2024) 493–500, https://doi.org/10.1038/s41586-024-07487-w.
[34] M.A.C. Neves, M. Totrov, R. Abagyan, Docking and scoring with ICM: the benchmarking results and strategies for improvement, J. Comput. Aided Mol. Des. 26 (6) (2012) 675–686, https://doi.org/10.1007/s10822-012-9547-0.
[35] S. Kumar, G. Stecher, M. Suleski, M. Sanderford, S. Sharma, K. Tamura, MEGA12: molecular evolutionary genetic analysis version 12 for adaptive and green computing, Mol. Biol. Evol. 41 (12) (2024) 1–9, https://doi.org/10.1093/molbev/msae263.
[36] S.Q. Le, O. Gascuel, An improved general amino acid replacement matrix, Mol. Biol. Evol. 25 (7) (2008) 1307–1320, https://doi.org/10.1093/molbev/msn067.
[37] D. Lu, M. Grant, B.L. Lim, NAD(H) and NADP(H) in plants and mammals, Mol. Plant 18 (6) (2025) 938–959, https://doi.org/10.1016/j.molp.2025.05.004.
[38] U. Zaman, R. Naz, N.S. Khattak, K.u. Rehman, A. Saeed, M. Farooq, J. Sahar, A. Iqbal, Kinetic and thermodynamic studies of novel acid phosphates extracted from *Cichorium intybus* seedlings, Int. J. Biol. Macromol. 168 (2021) 195–204, https://doi.org/10.1016/j.ijbiomac.2020.12.032.
[39] A.M. Olland, K.W. Underwood, R.M. Czerwinski, M.-C. Lo, A. Aulabaugh, J. Bard, M.L. Stahl, W.S. Somers, F.X. Sullivan, R. Chopra, Identification, characterization, and crystal structure of Bacillus subtilis nicotinic acid mononucleotide adenylyltransferase, J. Biol. Chem. 277 (5) (2002) 3698–3707, https://doi.org/10.1074/jbc.M109670200.
[40] I.A. Rodionova, B.M. Schuster, K.M. Guinn, L. Sorci, D.A. Scott, X. Li, I. Kheterpal, C. Shoen, M. Cynamon, C. Locher, E.J. Rubin, A.L. Osterman, Metabolic and bactericidal effects of targeted suppression of NadD and NadE enzymes in mycobacteria, mBio 5 (1) (2014) e00747-00713, https://doi.org/10.1128/mBio.00747-13.
[41] H. Zhang, T. Zhou, O. Kurnasov, S. Cheek, N. Grishin, A. Osterman, Crystal structures of *E. coli* nicotinate mononucleotide adenylyltransferase and its complex with deamido-NAD, Structure 10 (1) (2002) 69–79, https://doi.org/10.1016/S0969-2126(01)00693-1.
[42] L. Sorci, I.K. Blaby, I.A. Rodionova, J. De Ingeniis, S. Tkachenko, V. de Crecy-Lagard, A.L. Osterman, Quinolinate salvage and insights for targeting NAD biosynthesis in group a streptococci, J. Bacteriol. 195 (4) (2013) 726–732, https://doi.org/10.1128/JB.02002-12.
[43] L. Sorci, Y. Pan, Y. Eyobo, I. Rodionova, N. Huang, O. Kurnasov, S. Zhong, A. D. MacKerell Jr., H. Zhang, A.L. Osterman, Targeting NAD biosynthesis in bacterial pathogens: structure-based development of inhibitors of nicotinate mononucleotide adenylyltransferase NadD, Chem. Biol. 16 (8) (2009) 849–861, https://doi.org/10.1016/j.chembiol.2009.07.006.
[44] M.G. Rossman, A. Liljas, C.-I. Brändén, L.J. Banaszak, Evolutionary and structural relationships among dehydrogenases, in: P.D. Boyer (Ed.), The Enzymes, Academic

Press, Oxford, 1975, pp. 61–102, https://doi.org/10.1016/S1874-6047(08)60210-3.
[45] L. Holm, Dali server: structural unification of protein families, Nucleic Acids Res. 50 (W1) (2022) W210–W215, https://doi.org/10.1093/nar/gkac387.
[46] S. Han, M.D. Forman, P. Loulakis, M.H. Rosner, Z. Xie, H. Wang, D.E. Danley, W. Yuan, J. Schafer, Z. Xu, Crystal structure of nicotinic acid mononucleotide adenylyltransferase from *Staphylococcus aureus*: structural basis for NaAD interaction in functional dimer, J. Mol. Biol. 360 (4) (2006) 814–825, https://doi.org/10.1016/j.jmb.2006.05.055.
[47] S. Garavaglia, I. D'Angelo, M. Emanuelli, F. Carnevali, F. Pierella, G. Magni, M. Rizzi, Structure of human NMN adenylyltransferase: a key nuclear enzyme for NAD homeostasis, J. Biol. Chem. 277 (10) (2002) 8524–8530, https://doi.org/10.1074/jbc.M111589200.
[48] X. Ma, Y. Zhu, J. Lu, J. Xie, C. Li, W.S. Shin, J. Qiang, J. Liu, S. Dou, Y. Xiao, C. Wang, C. Jia, H. Long, J. Yang, Y. Fang, L. Jiang, Y. Zhang, S. Zhang, R.G. Zhai, C. Liu, D. Li, Nicotinamide mononucleotide adenylyltransferase uses its NAD(+) substrate-binding site to chaperone phosphorylated Tau, eLife 9 (2020) e51859, https://doi.org/10.7554/eLife.51859.
[49] I.A. Rodionova, H.J. Zuccola, L. Sorci, A.E. Aleshin, M.D. Kazanov, C.-T. Ma, E. Sergienko, E.J. Rubin, C.P. Locher, A.L. Osterman, Mycobacterial nicotinate mononucleotide adenylyltransferase: structure, mechanism, and implications for drug discovery, J. Biol. Chem. 290 (12) (2015) 7693–7706, https://doi.org/10.1074/jbc.M114.628016.
[50] V. Saridakis, E.F. Pai, Mutational, structural, and kinetic studies of the ATP-binding site of methanobacterium thermoautotrophicum nicotinamide mononucleotide Adenylyltransferase, J. Biol. Chem. 278 (36) (2003) 34356–34363, https://doi.org/10.1074/jbc.M205369200.
[51] S.Y. Gerdes, O.V. Kurnasov, K. Shatalin, B. Polanuyer, R. Sloutsky, V. Vonstein, R. Overbeek, A.L. Osterman, Comparative genomics of NAD biosynthesis in cyanobacteria, J. Bacteriol. 188 (8) (2006) 3012–3023, https://doi.org/10.1128/jb.188.8.3012-3023.2006.
[52] J. Mares, P. Hrouzek, R. Kana, S. Ventura, O. Strunecky, J. Komarek, The primitive thylakoid-less cyanobacterium gloeobacter is a common rock-dwelling organism, PLoS One 8 (6) (2013) e66323, https://doi.org/10.1371/journal.pone.0066323.
[53] J.A.G. Ochoa de Alda, R. Esteban, M.L. Diago, J. Houmard, The plastid ancestor originated among one of the major cyanobacterial lineages, Nat. Commun. 5 (1) (2014) 4937, https://doi.org/10.1038/ncomms5937.
[54] L. Hunt, F. Lerner, M. Ziegler, NAD - new roles in signalling and gene regulation in plants, New Phytol. 163 (1) (2004) 31–44, https://doi.org/10.1111/j.1469-8137.2004.01087.x.
[55] C.H. Foyer, G. Noctor, Redox regulation in photosynthetic organisms: signaling, acclimation, and practical implications, Antioxid. Redox Signal. 11 (4) (2008) 861–905, https://doi.org/10.1089/ars.2008.2177.
[56] P. Pétriacq, L. de Bont, G. Tcherkez, B. Gakière, NAD: not just a pawn on the board of plant-pathogen interactions, Plant Signal. Behav. 8 (1) (2013) e22477, https://doi.org/10.4161/psb.22477.
[57] A. Fernie, S.N. Hashida, K. Yoshimura, B. Gakiere, Z. Mou, P. Petriacq, Editorial: NAD metabolism and signaling in plants, Front. Plant Sci. 11 (2020) 146, https://doi.org/10.3389/fpls.2020.00146.
[58] X.-Q. Zheng, C. Nagai, H. Ashihara, Pyridine nucleotide cycle and trigonelline (N-methylnicotinic acid) synthesis in developing leaves and fruits of Coffea arabica, Physiol. Plant. 122 (4) (2004) 404–411, https://doi.org/10.1111/j.1399-3054.2004.00422.x.
[59] M.-B. Mititelu, O. Hudeček, A. Gozdek, R. Benoni, O. Nešuta, S. Krasnodębski, J. Kufel, H. Cahová, Arabidopsis thaliana NudiXes have RNA-decapping activity, RSC Chem. Biol. 4 (3) (2023) 223–228, https://doi.org/10.1039/D2CB00213B.
[60] K. Yoshimura, S. Shigeoka, Versatile physiological functions of the Nudix hydrolase family in Arabidopsis, Biosci. Biotechnol. Biochem. 79 (3) (2015) 354–366, https://doi.org/10.1080/09168451.2014.987207.
[61] K. Harada, Y. Nambu, S. Mizuno, T. Tsuge, In vivo and in vitro characterization of hydrophilic protein tag-fused Ralstonia eutropha polyhydroxyalkanoate synthase, Int. J. Biol. Macromol. 138 (2019) 379–385, https://doi.org/10.1016/j.ijbiomac.2019.07.095.
[62] T. Majtan, J.P. Kraus, Folding and activity of mutant cystathionine β-synthase depends on the position and nature of the purification tag: characterization of the R266K CBS mutant, Protein Expr. Purif. 82 (2) (2012) 317–324, https://doi.org/10.1016/j.pep.2012.01.019.
[63] L. Liu, F. Zhang, G. Li, G. Wang, Qualitative and quantitative NAD(+) metabolomics lead to discovery of multiple functional nicotinate N-glycosyltransferase in arabidopsis, Front. Plant Sci. 10 (2019) 1164, https://doi.org/10.3389/fpls.2019.01164.
[64] E.N. Smith, M. Schwarzländer, R.G. Ratcliffe, N.J. Kruger, Shining a light on NAD- and NADP-based metabolism in plants, Trends Plant Sci. 26 (10) (2021) 1072–1086, https://doi.org/10.1016/j.tplants.2021.06.010.
[65] L. Galeazzi, P. Bocci, A. Amici, L. Brunetti, S. Ruggieri, M. Romine, S. Reed, A. L. Osterman, D.A. Rodionov, L. Sorci, N. Raffaelli, Identification of nicotinamide mononucleotide deamidase of the bacterial pyridine nucleotide cycle reveals a novel broadly conserved amidohydrolase family, J. Biol. Chem. 286 (46) (2011) 40365–40375, https://doi.org/10.1074/jbc.M111.275818.
[66] L. Sorci, L. Brunetti, L. Cialabrini, F. Mazzola, M.D. Kazanov, S. D'Auria, S. Ruggieri, N. Raffaelli, Characterization of bacterial NMN deamidase as a Ser/Lys hydrolase expands diversity of serine amidohydrolases, FEBS Lett. 588 (6) (2014) 1016–1023, https://doi.org/10.1016/j.febslet.2014.01.063.
[67] L. Jaroszewski, L. Rychlewski, Z. Li, W. Li, A. Godzik, FFAS03: a server for profile–profile sequence alignments, Nucleic Acids Res. 33 (Web Server issue) (2005) W284–W288, https://doi.org/10.1093/nar/gki418.
[68] S. Sharma, Y.C. Hsieh, J. Dietze, M. Bockwoldt, O. Stromland, M. Ziegler, I. Heiland, Early evolutionary selection of NAD biosynthesis pathway in bacteria, Metabolites 12 (7) (2022) 569, https://doi.org/10.3390/metabo12070569.